ENVIRONMENTAL RESEARCH
LETTERS

PURPOSE-LED PUBLISHING™ Part of the ENVIRONMENTAL RESEARCH SERIES

LETTER • OPEN ACCESS

Emergent constraints on the future East Asian winter surface air temperature changes

To cite this article: Anqi Liu *et al* 2024 *Environ. Res. Lett.* **19** 064050

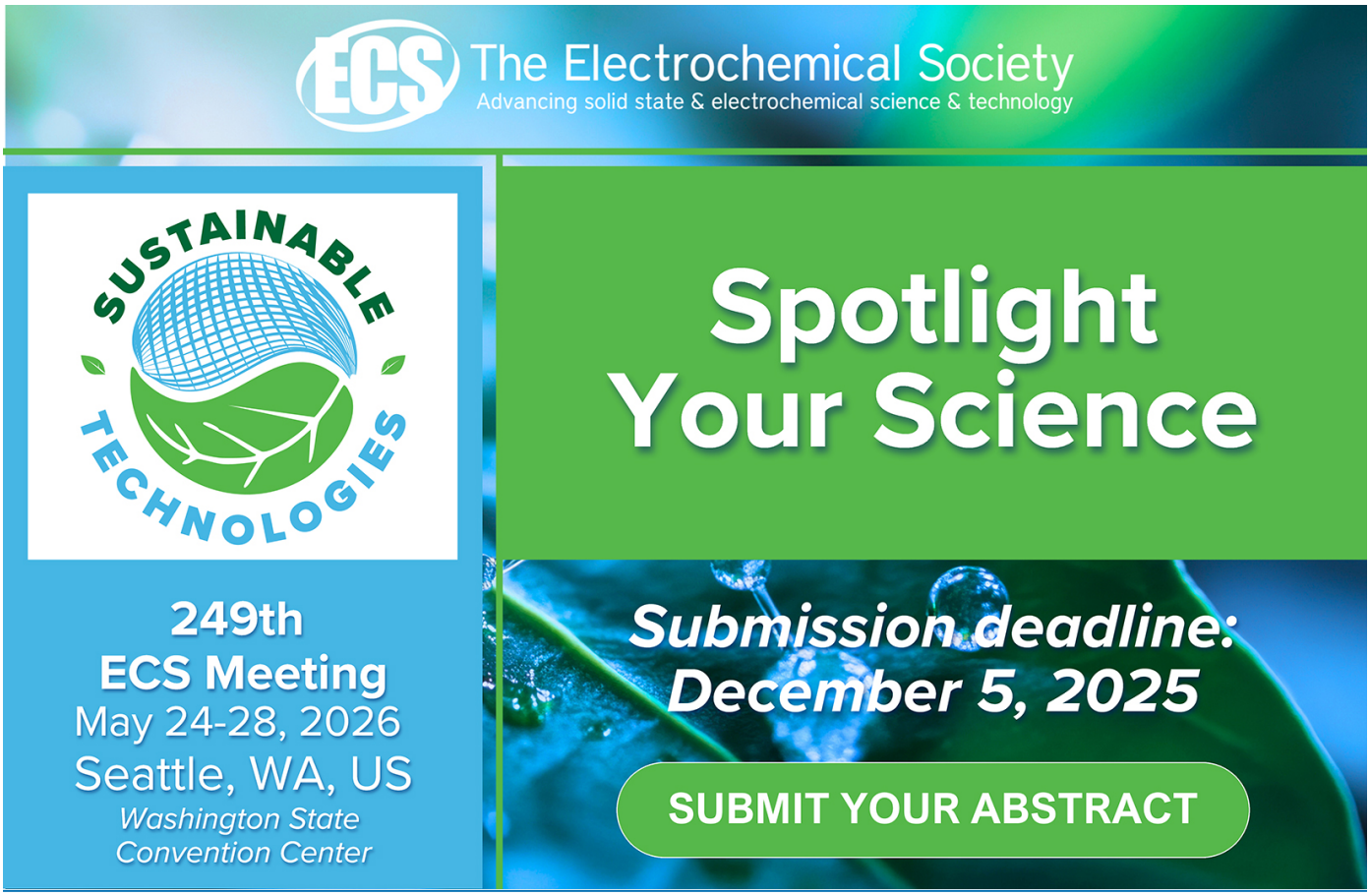

ENVIRONMENTAL RESEARCH
LETTERS

OPEN ACCESS

RECEIVED
18 January 2024

REVISED
22 April 2024

ACCEPTED FOR PUBLICATION
13 May 2024

PUBLISHED
29 May 2024

LETTER

Emergent constraints on the future East Asian winter surface air temperature changes

Anqi Liu[1], **Daokai Xue**[1], **Xiaolong Chen**[2,*] **and Danqing Huang**[1,*]

[1] School of Atmospheric Sciences, Nanjing University, Nanjing 210023, People's Republic of China
[2] State Key Laboratory of Numerical Modeling for Atmospheric Sciences and Geophysical Fluid Dynamics, Institute of Atmospheric Physics, Chinese Academy of Sciences, Beijing, People's Republic of China
* Authors to whom any correspondence should be addressed.

E-mail: chenxiaolong@mail.iap.ac.cn and huangdq@nju.edu.cn

Keywords: CMIP6, model uncertainties, constraints, East Asia, winter surface air temperature

Supplementary material for this article is available online

Abstract

In East Asia, the climate variability in boreal winter is dominated by the East Asian winter monsoon, one of the most energetic monsoon systems that can lead to disasters. The key variable, the East Asian winter surface air temperature (SAT), has significantly changed over the past century and has substantially impacted agriculture, ecosystems, economics, and public health. However, its projections are limited by considerable uncertainties. Here, we identify the first leading mode that explains almost 29.6% of the inter-model spread in future SAT change. Our research delves into the evolution of present-day biases under future scenarios and their consequential impact on the SAT. Models with stronger western currents' heat transport in the North Pacific exhibit a warmer North Pacific at mid-latitudes during historical periods. Additionally, these models consistently demonstrate stronger western currents in the future, contributing to the amplified warming of the western North Pacific, thereby warming Eurasia via the weakened trough and subtropical jet through barotropic responses to the warm North Pacific. Incorporating observational sea surface temperature constraints reduces uncertainties by 9.40%, revealing a more reliable SAT change pattern by the end of the 21st century.

1. Introduction

The East Asian winter monsoon (EAWM), a coupled extratropical–tropical system, represents the principal climatic component in East Asia during boreal winter. The surface air temperature (SAT), as the key variable of the EAWM system, serves as a crucial indicator of winter weather severity (Wang *et al* 2010). Its variations have significant economic implications, underscoring the critical need for reliable winter SAT projections to facilitate regional climate adaptation for policymakers (Han and Sun 2018). Previous studies have linked the EAWM to local forcings (Miao *et al* 2018), including the sea surface temperature (SST) over the North Pacific, which contributes to the decadal variability of the EAWM (Sun *et al* 2016) and remote forcing (Ding *et al* 2014, Wang and Chen 2014). Due to the complex mechanism, projections are still challenging due to the large uncertainty (Yao *et al* 2016, Monerie *et al* 2020, Aru *et al* 2021, Xue *et al* 2023), exhibiting a large spread across state-of-the-art Earth system models used for future projections (Fan *et al* 2020, Hu *et al* 2020, Xu *et al* 2022).

The Emergent Constraints (EC), which involve statistical relationships between the observation of the current climate and future changes among models, offer a potential means of reducing uncertainties in future projections by combining emergent relationships with observations (Hall *et al* 2019). However, to establish convincible EC, it is essential to clearly understand the underlying physical mechanisms that drive these statistical relationships (Chen *et al* 2020, Schlund *et al* 2020, Shiogama *et al* 2022). Although some studies have constrained regional climate uncertainties, such as constraints on the South Asian summer monsoon (Huang *et al* 2020b) and annual mean and extreme warming in China using

observed global warming (Chen *et al* 2023), limited attention is paid to the East Asian winter SAT uncertainties, excluding the effect of global warming, i.e. concerning local variations per 1 K of global warming.

Reducing uncertainties in temperature estimations for East Asia is more challenging compared to the global temperature estimations (Zhou and Yu 2006). This is because the regional temperature variations in East Asia are affected by multiple factors, making it more difficult to capture their overall characteristics. While previous studies have endeavored to constrain global temperature projections by relying on historical temperature trends (Jiménez-de-la-Cuesta and Mauritsen 2019, Nijsse *et al* 2020, Tokarska *et al* 2020), the regional characteristics of East Asia cannot be adequately represented by such constraints. Notably, our previous studies suggested that the regional SST exerts considerable influence on the winter SAT model spread both in the contemporary period (Liu *et al* 2022) and in the warming future (Liu *et al* 2023). Hence, it is critical to investigate whether the recent regional SST patterns can effectively narrow the model spread in future projections of winter SAT across East Asia.

In this study, we focus on the patterns of SAT change within transient and near-equilibrium responses (Rose *et al* 2014, Rose and Rayborn 2016, Dai *et al* 2020) instead of solely evaluating the extent of change at specific locations, which inherently hinges on radiative forcing and internal feedback. Consequently, our attention is channelled toward the normalization of change patterns by the global mean warming rate (Santer *et al* 1990, Tebaldi and Arblaster 2014). Here, we concentrate on how the SST biases in the present day evolve under the future scenario and thus influence SAT. We show that the SST biases in model simulations of the historical climate in the North Pacific are closely linked with the inter-model spread of future East Asian SAT projections in winter. By utilizing the constraint imposed by the SST on the winter East Asian SAT, the resultant constraint could elevate the accuracy of projections and provide insight into climate policies.

2. Data and methods

2.1. Data

We analyze the simulations from historical and shared socioeconomic pathway (SSP) 2–4.5 experiments using 36 coupled general circulation models participating in the CMIP6 (Eyring *et al* 2016). Table S1 in the supplementary material presents the names of the models, modeling groups (or centers), numbers of ensembles, and their letter labels. We utilize all available ensemble members for each model, encompassing relevant monthly atmospheric and oceanic variables (SST; sea potential temperature; sea water velocity), as well as radiation fluxes, for both the historical and projected data up to the end of the 21st century. The radiation fluxes include upward longwave radiation from the surface (R_{LU}), downwelling longwave radiation from above (R_{LD}), net solar radiation absorbed by the surface (R_{S}), and surface upward latent and sensible heat fluxes (LH and SH, respectively). All the model data are interpolated onto a horizontal 1 $\times 1^{\circ}$ grid. The multi-model mean (MMM) is determined by calculating the arithmetic mean of the 36 model simulations. Our study focuses on the climatological SAT changes in the boreal winter (December–January–February) during 2071–2100, relative to those during 1981–2014. The future changes in each variable investigated in our study are normalized by the global mean of winter SAT change in each model, which removes the effect of the inter-model uncertainty from the climate sensitivity in each model, as discussed by Huang *et al* (2020a) and Zhou *et al* (2020). The patterns of variable changes undergo normalization concerning local variations per 1 K of global warming, subsequently serving as metrics for quantifying the externally induced alterations in spatial distribution (Bellomo *et al.*, 2021).

Three observational SST datasets, namely, the Hadley Centre Sea Ice and SST data set (HadISST1) (Rayner *et al* 2003), NOAA extended reconstructed SST version 5 (ERSSTv5) (B. Huang *et al* 2017), and monthly mean Centennial *In Situ* Observation-Based Estimates of the Variability of Sea Surface Temperature version 2 (COBE-SST2), are used to constrain the uncertainty modes of winter Eurasian SAT projections (Hirahara *et al* 2014). The same period (1981–2014) as the model baseline is used to calculate the mean state of the observations. All the data are remapped onto a 1° grid by bilinear interpolation.

2.2. Methods

The conventional inter-model empirical orthogonal function (EOF) method is applied to the model-spatial dimension within the spatial domain of (20–53° N, 73–145° E) over land. This approach is employed to examine the primary modes of inter-model uncertainty in projecting SAT changes, and the eigenvalue in each mode is merged in the corresponding EOF (Chen *et al* 2020) utilizing the following calculation:

$$\Delta \mathrm{SAT}'(m,s) \cong \sum_{1}^{n} (\mathrm{PC}_{i,m} \times \mathrm{EOF}_{i,s}) \qquad (1)$$

in which Δ denotes the projected changes, m is the model number, s is the spatial grid, and n is the mode number. Prime represents the deviation from the multi-model ensemble mean. Here, the PCs are normalized.

A hierarchical framework rooted in robust statistical theory was proposed for EC (Bowman *et al* 2018). The first step of this framework involves establishing a relationship between future climate change (Y) and current climate (X) to constrain the uncertainty in Y. This relationship is derived by the climate model ensembles to approximate a linear relationship between Y and X.

$$Y = \overline{Y} + r\left(X - \overline{X}\right), \tag{2}$$

where $r = \frac{\sigma_Y}{\sigma_X}\rho$ is the regression coefficient, ρ is the correlation coefficient between Y and X, σ_Y and σ_X are the standard deviations of Y and X across models, respectively; and $\overline{X}$ and $\overline{Y}$ are MMMs. In this study, Y is the first normalized leading PC (PC1) (i.e., $\overline{Y} = 0$ and $\sigma_Y = 1$), and X is the corresponding SST pattern index.

Assuming a Gaussian distribution and an additive-noise model connecting observations to the current climate, the signal-to-noise ratio (SNR) in the observed current climate X_o can be derived. $\frac{1}{1+\mathrm{SNR}^{-1}}$ is then multiplied by a scaling factor r to make the necessary correction, where $\mathrm{SNR} = \sigma_X^2/\sigma_O^2$. Here, σ_X^2 is estimated by the variance across models and σ_O^2 is the variance across the three observational datasets. Equation (2) combined with the SNR correction, constrained expectation, and variability of future climate change $\overline{Y}_C$ can be expressed as follows:

$$\overline{Y}_c = \overline{Y} + \frac{r}{1+\mathrm{SNR}^{-1}}\left(\overline{X}_o - \overline{X}\right) \tag{3}$$

$$\sigma_{\overline{Y}_c}^2 = \left(1 - \frac{\rho^2}{1+\mathrm{SNR}^{-1}}\right)\sigma_{\overline{Y}}^2. \tag{4}$$

Therefore, the complete reduction in model variance achieved in this investigation by restricting PC1 can be expressed as a weightage of their corresponding explained variances, namely, PCV1, as a percentage:

$$\mathrm{TRV} = \frac{\rho^2}{1+\mathrm{SNR}^{-1}}\mathrm{PCV1}. \tag{5}$$

If the $\mathrm{SNR} \gg 1$, the reduced variance is determined by only ρ, or the impact of the SNR cannot be neglected.

The EC calculates the optimal values of PC1 by utilizing the observed SST pattern. Subsequently, the EOF reconstruction technique is employed to rectify the projection of the winter Eurasian SAT according to equation (1):

$$\Delta\mathrm{SAT} = \overline{\Delta\mathrm{SAT}} + \Delta\mathrm{SAT}' \approx \overline{\Delta\mathrm{SAT}} + \sum_{1}^{n}\left(\mathrm{PC}_{i,O} \times \mathrm{EOF}_{i,s}\right) \tag{6}$$

in which subscript 'O' denotes optimal PCs constrained by observational SST. Here, the mode number n is 1. The sea level pressure and 850 hPa wind fields can be corrected using a similar approach as in equation (6), but replacing the EOF terms with regression coefficients associated with PC1.

Since the R_{LU} is determined by surface temperature according to the Stefan–Boltzmann law, diagnosis of R_{LU} based on surface energy balance can be used to understand how SST anomalies are produced. Furthermore, in this framework, the oceanic heat transport (OHT) resulting from ocean dynamics is simply derived as a residual term:

$$R_{\mathrm{LU}} = R_{\mathrm{LD}} + R_{\mathrm{S}} + \mathrm{LH} + \mathrm{SH} + \mathrm{OHT}, \tag{7}$$

in which the positive direction is upward only for R_{LU}, but downward onto surface for other terms. Moreover, we also directly calculate the internal energy advection in oceanic mixed layer to estimate the OHT as follows:

$$\mathrm{OHT} = -\rho C_p \int_{-h}^{0} \vec{U}\cdot\nabla T\mathrm{d}z - \rho C_p \int_{-h}^{0} W\frac{\partial T}{\partial z}\mathrm{d}z + \mathrm{res} \tag{8}$$

in which the lower bound of vertical integral h is 200 m, representing the typical depth of mixed layer in the mid-latitude North Pacific. The horizontal sea water velocities (uo, vo) and the vertical velocity (wo) are represented by U and W, respectively. The zonal, meridional and vertical heat transport are defined as Qx, Qy and Qz, respectively. The specific heat at constant pressure, denoted as C_{p}, is 4000 $J\ \mathrm{kg}^{-1}{}^{\circ}\mathrm{C}^{-1}$. The potential density, ρ, is considered constant ($=$1035 $\mathrm{kg\,m}^{-3}$) for the region studied due to its minimal variation (less than 2%) across the range of temperature and salinity.

2.3. Definition of indices

Following Chen *et al* (2020), we calculate the SST pattern index, T1, by projecting the historical mean state SST in boreal winter in each model ($\mathrm{SST}_{\mathrm{hist}}$) onto the inter-model anomalous SST ($\mathrm{SST}'_{\mathrm{PC1}}$) (figure 3(b)). To more clearly reflect the SST patterns, we use large domains rather than local areas. T1 quantifies the historical SST distributions of the western North Pacific region (17°–37° N, 120° E–160° W) as follows:

$$\mathrm{T1} = \mathrm{SST}_{\mathrm{hist}} \cdot \mathrm{SST}'_{\mathrm{PC1}}\left(17^{\circ}-37^{\circ}\mathrm{N}, 120^{\circ}\mathrm{E}-160^{\circ}\mathrm{W}\right). \tag{9}$$

Observational T1 values are derived from three distinct SST datasets.

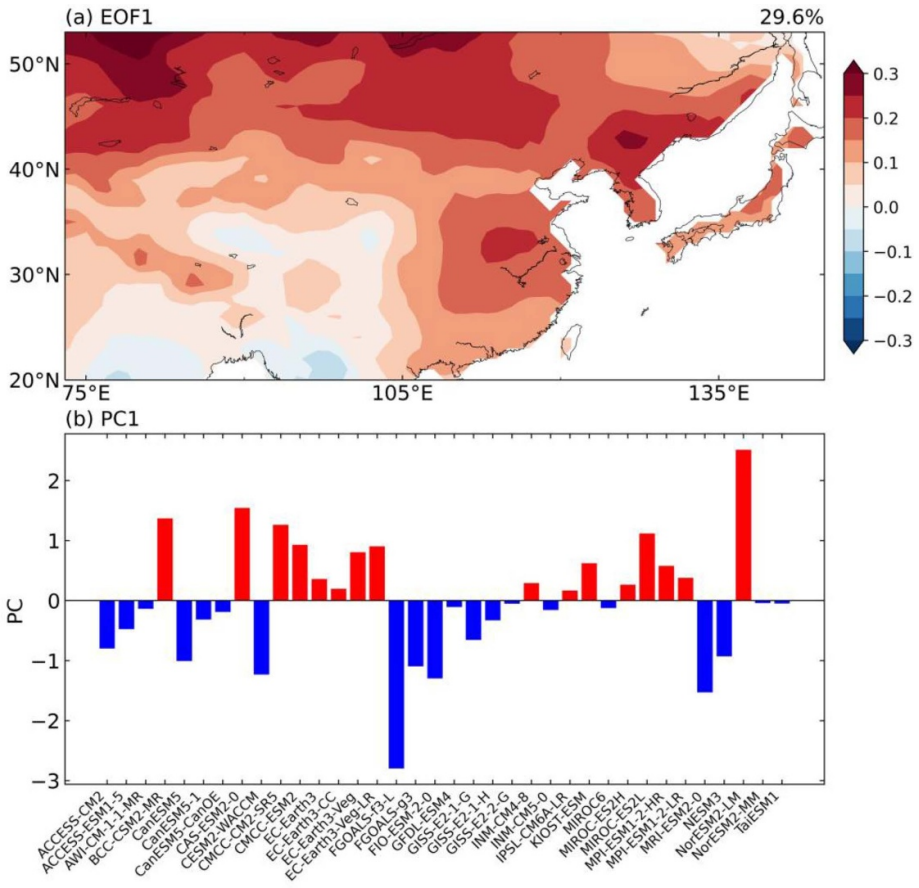

Figure 1. (a) The first leading mode (EOF1) derived from inter-model EOF analysis of projected changes (in the boreal winter (December–January–February) during 2071–2100, relative to those during 1981–2014) in the winter East Asian surface air temperature (SAT; shaded; $K \cdot K^{-1}$). The value indicated in the top-right corner signifies the explained inter-model variance by the corresponding mode. (b) The corresponding principal component (PC1).

3. Results

3.1. Leading uncertainty mode in East Asian SAT changes and related physical processes

Based on the inter-model EOF analysis across 36 models, the leading modes of the projection uncertainties in the winter East Asian SAT changes have been derived. This study focused on the EOF1 and PC1, which accounted for 29.6% of the inter-model spread. The first leading uncertainty mode exhibited a spatially consistent warming change over the entire East Asian continent, resembling the southern mode revealed by Wang *et al* (2010), with several warming centers in Mongolia and the eastern coastal region (figure 1(a)), as previously demonstrated (Liu *et al* 2023). The pattern is also found under the SSP5-8.5 scenario (figure S1).

Here, we trace the leading SAT uncertainty modes back to specific ocean conditions and highlight the role of SST changes. The first leading mode is significantly related to the warming changes in the midlatitudes over the western North Pacific (figure 2(a)), consequently resulting in a poleward meridional temperature gradient (MTG) amplified by the increase in greenhouse gas concentrations (Yang *et al* 2022). According to the principles of thermal wind theory, the strength of the westerly will increase (decrease) over the area where the MTG increases (decreases) (figure 2(d)), corresponding to the previous studies (Liu *et al* 2022, Sun *et al* 2016). To further investigate the associated atmospheric circulations, we investigate the related atmospheric variables and observe that the equivalent barotropic positive height and anticyclonic anomalies cover the North Pacific (figures 2(b) and (c)). Furthermore, the weakened East Asian subtropical jet (figure 2(d)) is associated with diminished large-scale circulations (Mao *et al* 2007), including the weakened Siberian high and East Asian trough (figures 2(b) and (c)). These patterns can prevent cold anomalies over East Asia, leading to a weakened EAWM, as found in previous studies (Luo and Zhang 2015). Controlled by an unstable ocean-atmosphere interaction mechanism at midlatitudes through the heat flux from the ocean (Fang and Yang 2016, Sun *et al* 2016), barotropic responses promote warming SST anomalies via surface wind anomalies at midlatitudes (Toda and Watanabe 2020, p. 195, Yang *et al* 2022). The

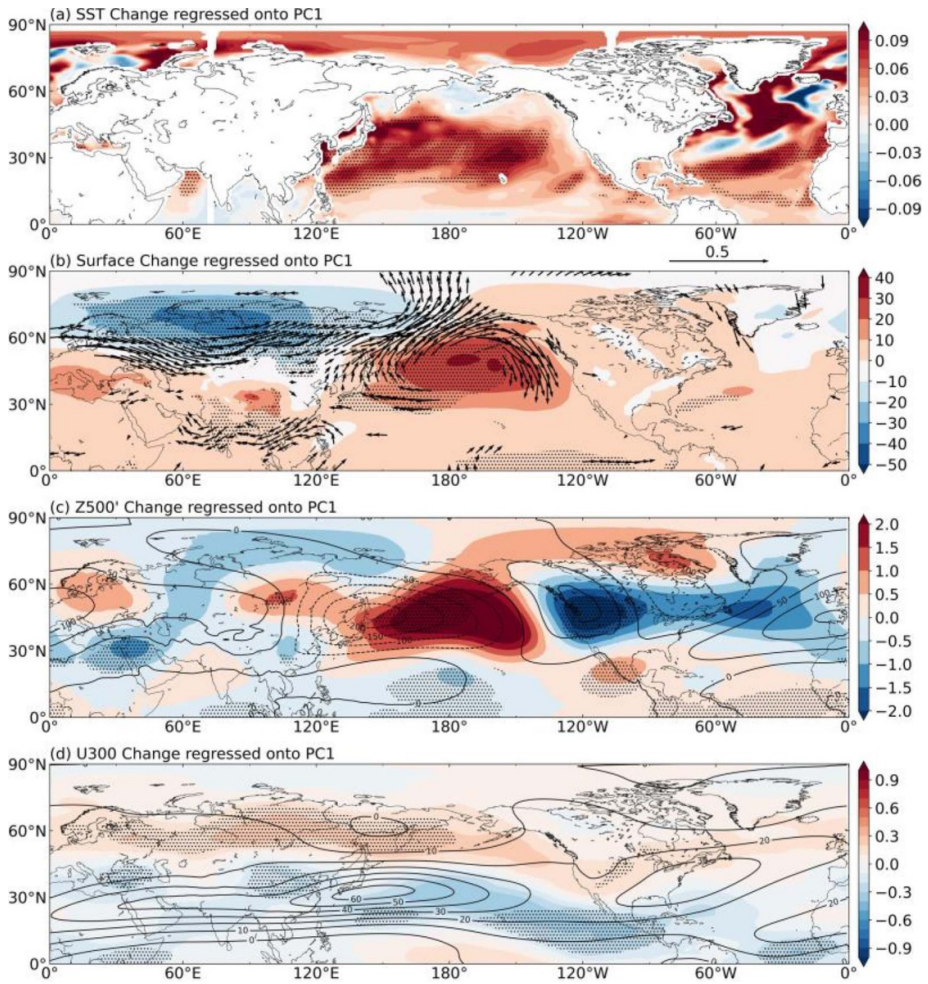

Figure 2. Inter-model spread in projected changes associated with the first principal component (PC1). (a) sea surface temperature (SST; shading; $K \cdot K^{-1}$). (b) sea level pressure (SLP; shading; $Pa \cdot K^{-1}$) and wind (vectors drawn for statistical significance at the 5% level under Student t test; $m \cdot s^{-1} \cdot K^{-1}$) at 850 hPa. (c) The 500 hPa eddy geopotential height field ($Z500'$; shadings; unit: $m \cdot K^{-1}$) and the historical multi-model mean (MMM) of the 500 hPa eddy geopotential height (contours; unit: m). (d) 300 hPa zonal wind (shadings; unit: $m \cdot s^{-1} \cdot K^{-1}$) and the historical MMM of 300 hPa zonal wind (contours; unit: $m \cdot s^{-1}$). Stippled regions are statistically significant at the 5% level according to Student's t test.

weakened subtropical jet, intensified mid-to-low latitude surface easterlies and weakened East Asian trough are all related to the barotropic responses (figures 2(b)–(d)), consistent with the results of sensitivity experiments in previous studies, identifying the role of midlatitude air-sea coupling (Sun *et al* 2016, Fang *et al* 2022). As a result, the weakened EAWM contributes to the first leading mode (figure 1(a)), corresponding to the circulation structures exhibited by the warming southern mode (Wang *et al* 2010). The anticyclone anomalies over the North Pacific prevent the cold-air intrusion along the eastern coastal region.

3.2. Tracing the origin of future SST changes spread back to historical sources

As previously discussed, SST anomalies impact atmospheric circulation, thus influencing the uncertainty of projection. Consequently, our objective is to trace the origins of these SST anomalies (figure 3(b)). To elucidate the origin of the spread of future SST changes, which influence East Asian SAT spread as previously mentioned, we investigate the main processes in the surface energy budget (equation (7)). First, the uncertainties in changes in surface radiation components related to PC1 are examined. The positive anomalies of R_{LU} (figure 4(a)), reflecting the warm SST anomalies (figure 2(a)), seem well explained by the R_{LD} which exhibits a similar spatial pattern and magnitude (figures 4(b) and 3(a)). However, the negative LH term can compensate to a large extent and other terms' contributions, such as the OHT, cannot be neglected. Hence, all these processes should be understood in a unified framework. Considering that processes such as radiations and air-sea fluxes can interact with each other, rather than being the causes of SST anomalies, starting from OHT, which also positively contributes to the SST uncertainty (figure 4(f)), is a reasonable approach. More OHT in the North Pacific (figure 4(f)) initially leads to higher

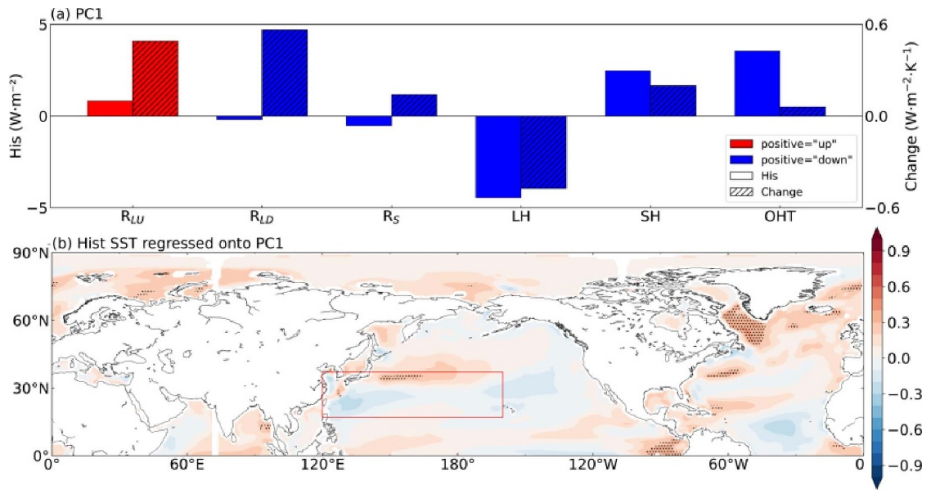

Figure 3. (a) The inter-model spread of radiation components (surface upwelling longwave radiation (R_{LU}), surface downwelling longwave radiation (R_{LD}), net shortwave surface radiation (R_S), surface upward latent heat flux (LH) surface upward sensible heat flux (SH), and oceanic heat transport (OHT)) in the western North Pacific at midlatitudes $(30^\circ - 50^\circ\,\mathrm{N}, 140^\circ\,\mathrm{E} - 180^\circ)$ in historical simulations (left bars) and future changes (right bars, hatched). Except for the 'R_{LU}' component, where an upward direction is considered positive, all the other components are defined with downward directions as positive. (b) Inter-model spread in historical sea surface temperature (SST; shadings; K) associated with the first principal component (PC1). The box in (b) is utilized to define the SST pattern index (17°–37° N, 120° E–160° W), i.e. T1, which subsequently helps in constraining the PC ('Methods'). Stippling indicates that the difference is statistically significant at the 10% level according to Student's t test.

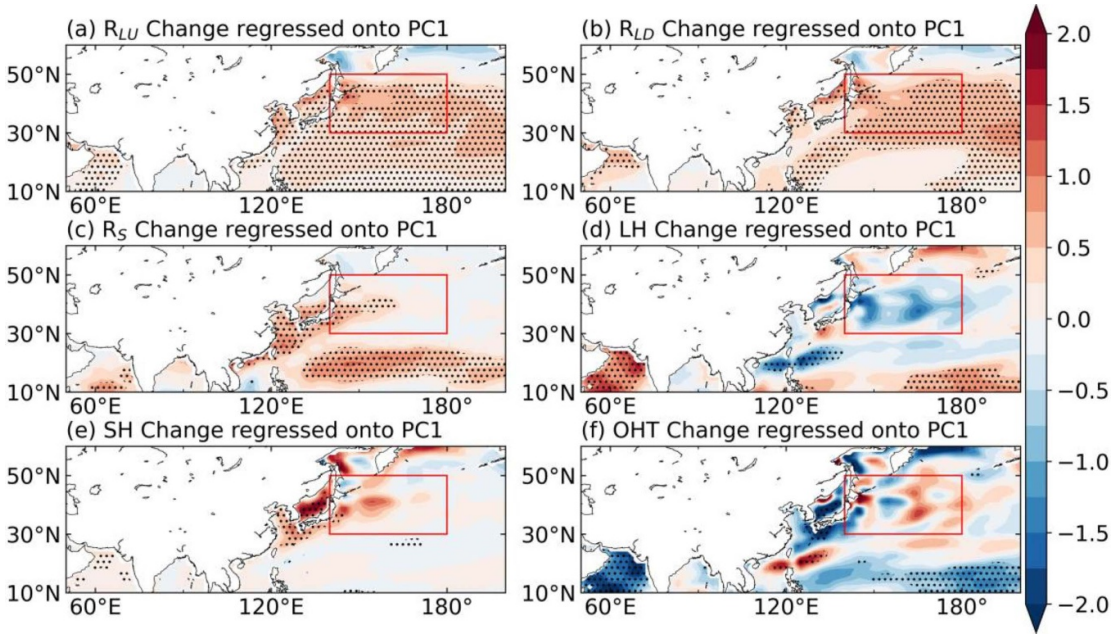

Figure 4. Inter-model spread in the radiation flux change associated with the first principal component (PC1). (a) Surface upwelling longwave radiation (R_{LU}); (b) surface downwelling longwave radiation (R_{LD}); (c) net shortwave surface radiation (R_S); (d) surface upward latent heat flux (LH); (e) surface upward sensible heat flux (SH); (f) oceanic heat transport (OHT)) $(\mathrm{W}\cdot\mathrm{m}^{-2}\cdot\mathrm{K}^{-1})$. Except for the '$R_{LU}$' component, where an upward direction is considered positive, all the other components are defined with downward directions as positive. Stippled regions are statistically significant at the 10% level according to Student's t test. The box is utilized to calculate the heat flux spread in the western North Pacific at midlatitudes$(30^\circ - 50^\circ\,\mathrm{N}, 140^\circ\,\mathrm{E} - 180^\circ)$ in figure 3(a).

SST but then more LH is released into the atmosphere and cooling the sea surface (figure 4(d)), which can be verified by the similar spatial patterns between these two terms. The water vapor evaporated into the atmosphere spreads to a larger domain in the North Pacific (figure S2) due to advection and mixing by the atmospheric circulations such as the climatological westerlies, and in turn, heats the sea surface through the downward longwave radiation (figure 4(b)) which finally becomes a dominant process leading to the North Pacific warming (figure 3(a)). Additionally, the magnified warming over the North Pacific is

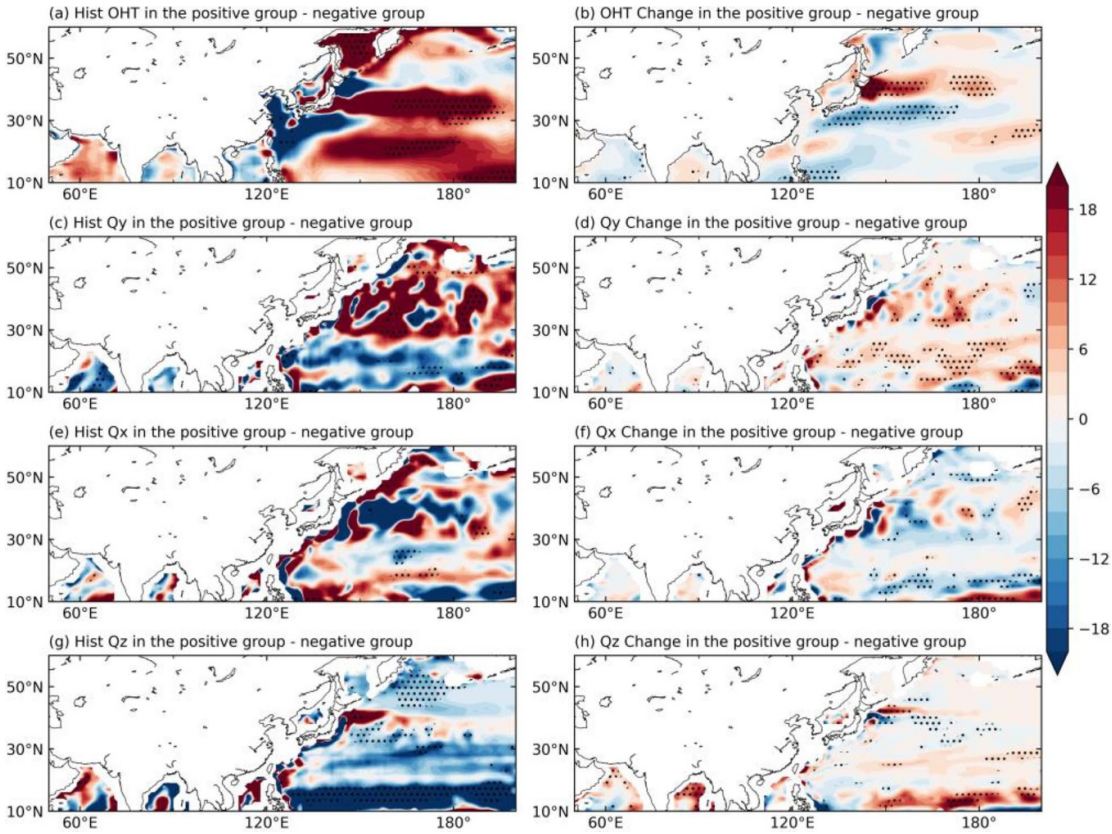

Figure 5. The difference in composite oceanic heat transport (OHT) (a, b), integrated meridional heat advection (Qy) (c), (d), zonal heat advection (Qx) (e), (f), and vertical heat advection (Qz) (g, h) between the positive and negative groups is shown for both the historical period (a), (c), (c), (g) ($W \cdot m^{-2}$) and future change (b), (d), (f), (h) ($W \cdot m^{-2} \cdot K^{-1}$). Stippled regions are statistically significant at the 10% level according to Student's t test.

also partly contributed by suppressed sensible heat flux (figures 4(e) and 3(a)) as well as more downward shortwave radiation (figures 4(c) and 3(a)), possibly caused by the responding anticyclone anomalies (figure 2(b)).

To more clearly show the related oceanic process, we selected models for the composite analysis based on the normalized PC1 to diagnose the internal heat advections in the mixed layer (equation (8)). The positive group (PC1 $\geqslant$ 1.0) has MIROC-ES2L and NorESM2-LM, while the negative group (PC1 $\leqslant -1.0$) has CanESM5, CESM2-WACCM, FGOALS-f3-L, FGOALS-g3, FIO-ESM-2-0, and MRI-ESM2-0. Compared to the negative group, the positive group shows a stronger OHT contribution to ocean warming in the future (figure 5(b)), in which stronger western North Pacific currents south of 30°N transport more heat to the mid-latitude western North Pacific (figure 5(d)), while the effects of zonal and vertical heat transport are smaller (figures 5(f) and (h)). We also decompose the meridional heat transport (figure 5(d)), and figure S2 demonstrates that the changes in ocean currents dominate the contribution. It is consistent with a previous study indicating that surface warming accelerates the subtropical gyres (Peng *et al* 2022).

This phenomenon, observed in the future, inherits from the historical period (figures 5(a) and (c)). The OHT is the dominant term contributing to the uncertainty of North Pacific SST related to PC1 in historical simulations (figure 3(a)). Models with stronger meridional heat transport along the western boundary (figure 5(c)) tend to show a warmer SST in the Kuroshio Extension while colder in the tropical region south to Japan (figure 3(b)). Briefly speaking, the stronger meridional OHT and warmer Kuroshio Extension observed in the historical period (figures 5(a) and (c)) correspond to a stronger increase in OHT and warming in the North Pacific in future projections (figures 5(b) and 2(a)), releasing energy and heating the overlying atmosphere. As discussed in section 3.1, this leads to a deceleration of the subtropical jet by weakening the MTG (figure 2(d)) and finally causes larger warming in East Asia (figure 2(a)).

3.3. Reducing uncertainties in the East Asian winter SAT using observational SST

As shown in the above section, the uncertainty pattern of climatological SST in historical simulations related to PC1 shows warm anomalies in the Kuroshio Extension while cold anomalies to the south (box in figure 3(b)), which is associated with stronger OHT

by the western boundary currents. Based on the relatively reliable SST observations and the established physical relationship above, the correlation between the SST pattern and the leading mode of inter-model spread allows ECs to be applied to the projection of the East Asian SAT. To derive a more robust projection than the conventional MMM, we utilize a well-established hierarchical statistical framework for EC (Bowman *et al* 2018). First, as defined above, T1 is generated to assess the model's skill in simulating the observed SST pattern during the historical period. This is achieved by projecting the mean-state SST onto the SST mode (box in figure 3(b)) associated with PC1, which measures the models' ability to capture the SST pattern and related OHT over the western North Pacific. We select the index not only due to its significance in figure 3(b) but also its relevance to future climate change, as carefully elucidated above. We also calculate the index for the three observational SST datasets to compare its average with those for each model.

Results show that T1 is higher than the observation in 86.11% of the models (figure 6(a)), indicating that most models overestimate the warming over the western North Pacific (figure 6(a)). These findings underscore the need for improved model simulations of SST in these key regions to reduce the uncertainty in the future projection of East Asian SAT.

In the hierarchical statistical framework with Gaussian assumptions, the slope r, which connects the historical predictor and future predictand, is subject to additional influence from the SNR of the observed current climate, as the observations are utilized in the constraints. When the SNR is significantly large (i.e. SNR $\gg$ 1), its impact on r can be disregarded. In the case of T1, the SNR is notably high, with a value of 82.93. This high SNR is attributed to the considerable consistency in the climatological SST patterns among the observational datasets. Therefore, the corrected regression line of PC1 remains largely unchanged from the original line.

Another important consequence of the hierarchical statistical framework is a relative reduction in variance after being constrained by observations. For PC1, the reduced variance is approximately 31.75% (figure 6), which is mainly determined by the high correlation coefficient with T1 (figure 6(a)) since the SNR is large enough. Considering the variance explained by PC1 (29.6%), the variance reduced by the ECs is about 9.40% (31.75% $\times$ 29.6%) based on equation (5).

We generate new projections by constraining the conventional MMM using the EOF and optimal PC1 (figure 6(b)). The present-day T1, as an EC, results in a cold SAT change pattern at the end of the 21st century, compared to the initial MMM (figure 6(c)). In contrast to the uncorrected results, the western North Pacific exhibits a low-pressure anomaly, corresponding to figure 2 (figure 6(c)). Consequently, aligning with figure 2(b), coastal East Asia experiences intensified northerly winds (figure 6(c)). In the constrained results, for every 1 K increase in global temperature, the temperature increase slows by 5.17% in East China (25–45° N, 105–120° E), 5.95% in Mongolia (41–52° N, 88–120° E), and 5.58% in the Korean peninsula and South Japan (30–45° N, 125–145° E), relative to the conventional MMM. The constrained projections provide a more reliable and robust outlook of the future climate change scenario, highlighting the importance of accounting for the EOF pattern and optimal PC in projecting regional climate change.

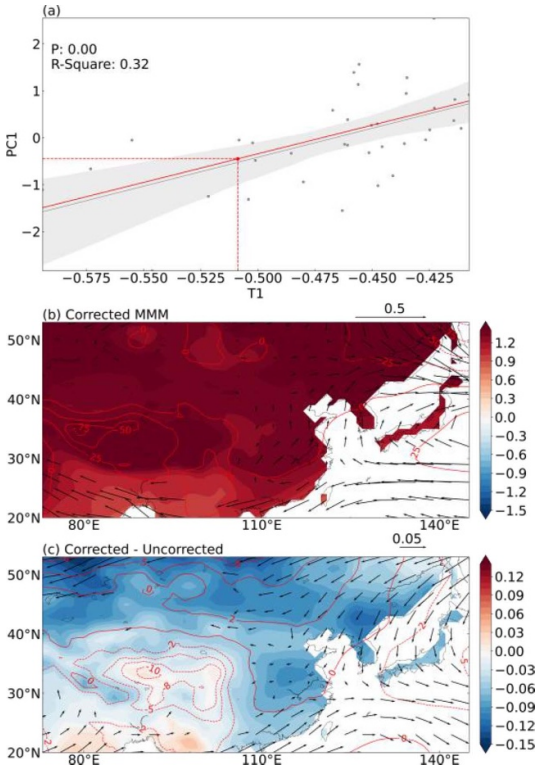

Figure 6. T1 in (a) (K) measures how the sea surface temperature (SST) patterns in the box in figure 3(e) are simulated in a model's historical climate. The y-coordinate and x-coordinate of the grey asterisk respectively denote the values of the corresponding principal component (PC) for each mode, as well as T1. The grey-shaded region represents the 95% confidence interval of the linear regression. The thin red line is an observational correction based on equation (3). The means of the three observational results (from HadISSTv1.1, ERSSTv5, and COBE-SST2) yield the optimal constraint (red dashed line). The values in the left corner of each subplot are the p value and R-square. (b) Corrected winter East Asian surface air temperature projection (SAT; shadings; $\mathrm{K}\cdot\mathrm{K}^{-1}$) and related changes in 850 hPa wind (vectors; $\mathrm{m}\cdot\mathrm{s}^{-1}\cdot\mathrm{K}^{-1}$) and sea level pressure (contours; $\mathrm{Pa}\cdot\mathrm{K}^{-1}$) in the multi-model ensemble mean (MMM) based on the best-estimated principal components ('Methods'). (c) The difference between the corrected and uncorrected results.

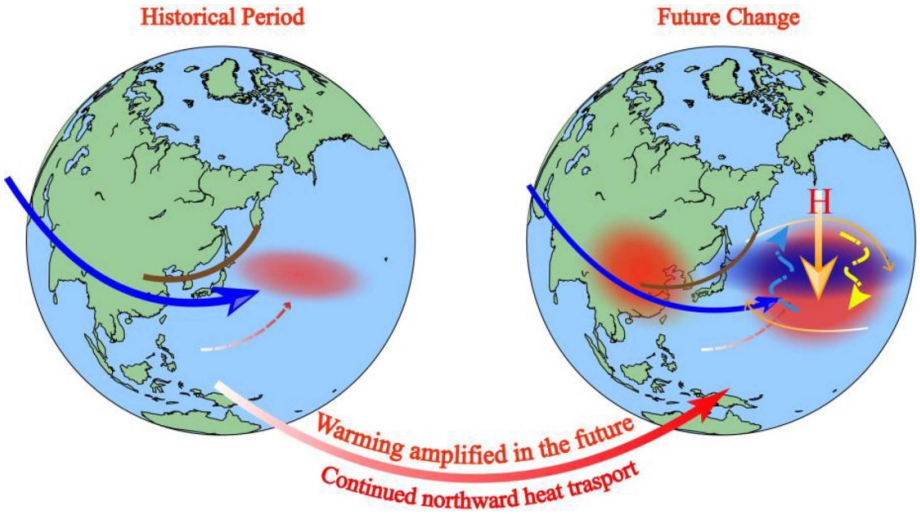

Figure 7. Schematic pictures for Emergent Constraint on winter East Asian surface air temperature (SAT). The left panel signifies the historical period, wherein the dashed red gradient arrow denotes northward heat transport, the blue curved arrow symbolizes a strong subtropical jet and the red circle represent warm SST. The right panel signifies the future change, wherein the dashed red gradient arrow denotes northward heat transport, the red circle represents the warming of East Asia and the western North Pacific, and the blue circle represents the released water vapor. The yellow straight arrow represents anomalous circulation patterns, while the blue curved arrow symbolizes a weakened subtropical jet. The wavy dashed blue arrow indicates upward latent heat flux, and the wavy dashed yellow arrow indicates downward longwave radiation. The letter 'H' designates positive barotropic anomalies, and the brown curve illustrates a weakened trough.

4. Conclusions and discussions

We suggest constraining the East Asian winter SAT change by correcting biases in the present-day SST over the North Pacific, leveraging the established relationship between them. In comparison to the original MMM, the corrected pattern indicates a significant weakening of the East Asian warming pattern. This weakening is attributed to the strengthening of the subtropical jet and the trough, accompanied by corresponding negative barotropic anomalies in a warming future. This approach reduces roughly 9.40% of the inter-model spread and reinforces the credibility of the projection. As shown in figure 7, the historically strong western currents over the North Pacific could affect the inter-model uncertainties over East Asia. These findings suggest that the inter-model spread in ocean dynamics could influence climate uncertainties in regions beyond East Asia, warranting further exploration in the future.

In our study, we analyze the source of the leading mode of winter East Asian SAT uncertainty from the perspective of the ocean's influence, thereby reducing the variance of the leading mode by approximately one third. However, other processes, such as land surface processes, may still contribute to the residual uncertainty. For instance, variations in soil moisture can directly affect SAT by altering the Bowen ratio (Eltahir 1998) and indirectly affect SAT by modifying atmospheric circulations (Shukla and Mintz 1982, Liu *et al* 2012). Therefore, future research should continue to explore the impacts of other processes on the uncertainty in winter SAT projection in East Asia.

Data availability statement

The CMIP6 model data used in this study can be accessed at the ESGF portal (https://esgf-node.llnl.gov/projects/esgf-llnl/), as mentioned in the citation (Eyring *et al* 2016) [dataset]; the HadISST datasets are available at www.bodc.ac.uk/data/information_and_inventories/edmed/report/1026026/ (Rayner *et al* 2003) [dataset]; the ERSSTv5 datasets are available at https://psl.noaa.gov/data/gridded/data.noaa.ersst.v5.html (Huang *et al* 2017) [dataset]; and the COBE-SST2 datasets are available at https://amaterasu.ees.hokudai.ac.jp/~ism/pub/cobe-sst2 (Hirahara *et al* 2014) [dataset]. The figures in this manuscript are prepared using Python software (URL: www.python.org/downloads/) [software].

The data that support the findings of this study are openly available at the following URL/DOI: https://doi.org/10.5194/gmd-9-1937-2016.

Acknowledgments

This study is jointly sponsored by the National Key Research and Development Program of China (Grants 2020YFA0608901 and 2020YFA0608904), the National Natural Science Foundation of China (Grant 42075020), and the Jiangsu Collaborative Innovation Center for Climate Change.

ORCID iDs

Xiaolong Chen https://orcid.org/0000-0003-4098-9952
Danqing Huang https://orcid.org/0000-0002-3112-0617

References

Aru H, Chen W and Chen S 2021 Is there any improvement in simulation of the wintertime western pacific teleconnection pattern and associated climate anomalies in CMIP6 compared to CMIP5 models? *J. Clim.* **34** 8841–61

Bellomo K, Angeloni M, Corti S and von Hardenberg J 2021 Future climate change shaped by inter-model differences in Atlantic meridional overturning circulation response *Nat. Commun.* **12** 3659

Bowman K W, Cressie N, Qu X and Hall A 2018 A hierarchical statistical framework for emergent constraints: application to snow-albedo feedback *Geophys. Res. Lett.* **45** 13050–9

Chen X, Zhou T, Wu P, Guo Z and Wang M 2020 Emergent constraints on future projections of the western North Pacific subtropical high *Nat. Commun.* **11** 2802

Chen Z, Zhou T, Chen X, Zhang W, Zuo M, Man W and Qian Y 2023 Emergent constrained projections of mean and extreme warming in China *Geophys. Res. Lett.* **50** e2022GL102124

Dai A, Huang D, Rose B E J, Zhu J and Tian X 2020 Improved methods for estimating equilibrium climate sensitivity from transient warming simulations *Clim. Dyn.* **54** 4515–43

Ding Y, Liu Y, Liang S, Ma X, Zhang Y, Si D, Liang P, Song Y and Zhang J 2014 Interdecadal variability of the East Asian winter monsoon and its possible links to global climate change *J. Meteorol. Res.* **28** 693–713

Eltahir E 1998 A soil moisture rainfall feedback mechanism 1. Theory and observations *Water Resour. Res.* **34** 765–76

Eyring V, Bony S, Meehl G A, Senior C A, Stevens B, Stouffer R J and Taylor K E 2016 Overview of the coupled model intercomparison project phase 6 (CMIP6) experimental design and organization *Geosci. Model. Dev.* **9** 1937–58

Fan X, Duan Q, Shen C, Wu Y and Xing C 2020 Global surface air temperatures in CMIP6: historical performance and future changes *Environ. Res. Lett.* **15** 104056

Fang J, Chen L and Yang X-Q 2022 Roles of vertical distributions of atmospheric transient eddy dynamical forcing and diabatic heating in midlatitude unstable air–sea interaction *Clim. Dyn.* **58** 351–68

Fang J and Yang X-Q 2016 Structure and dynamics of decadal anomalies in the wintertime midlatitude North Pacific ocean–atmosphere system *Clim. Dyn.* **47** 1989–2007

Hall A, Cox P, Huntingford C and Klein S 2019 Progressing emergent constraints on future climate change *Nat. Clim. Change* **9** 269–78

Han S and Sun J 2018 Impacts of autumnal Eurasian snow cover on predominant modes of boreal winter surface air temperature over Eurasia *J. Geophys. Res. Atmos.* **123** 10–076

Hirahara S, Ishii M and Fukuda Y 2014 Centennial-scale sea surface temperature analysis and its uncertainty *J. Clim.* **27** 57–75

Hu X, Fan H, Cai M, Sejas S A, Taylor P and Yang S 2020 A less cloudy picture of the inter-model spread in future global warming projections *Nat. Commun.* **11** 4472

Huang B, Thorne P W, Banzon V F, Boyer T, Chepurin G, Lawrimore J H, Menne M J, Smith T M, Vose R S and Zhang H-M 2017 Extended reconstructed sea surface temperature, version 5 (ERSSTv5): upgrades, validations, and intercomparisons *J. Clim.* **30** 8179–205

Huang D, Dai A and Zhu J 2020a Are the transient and equilibrium climate change patterns similar in response to increased CO_2? *J. Clim.* **33** 8003–23

Huang X, Zhou T, Dai A, Li H, Li C, Chen X, Lu J, Von Storch J-S and Wu B 2020b South Asian summer monsoon projections constrained by the interdecadal Pacific oscillation *Sci. Adv.* **6** eaay6546

Jiménez-de-la-Cuesta D and Mauritsen T 2019 Emergent constraints on Earth's transient and equilibrium response to doubled CO2 from post-1970s global warming *Nat. Geosci.* **12** 902–5

Liu A, Huang D and Huang A 2023 The leading intermodel spread of the projected changes in the Eurasian continent winter surface air temperature and large-scale circulations from the CMIP6 simulations *J. Geophys. Res. Atmos.* **128** e2023JD038829

Liu A, Huang Y and Huang D 2022 Inter-model spread of the simulated winter surface air temperature over the Eurasian Continent and the physical linkage to the jet streams from the CMIP6 models *J. Geophys. Res. Atmos.* **127** e2022JD037172

Liu G, Chen J, Ji L and Sun S 2012 Relationship of summer soil moisture with early winter monsoon and air temperature over eastern China *Int. J. Climatol.* **32** 1513–9

Luo X and Zhang Y 2015 The linkage between upper-level jet streams over East Asia and East Asian winter monsoon variability *J. Clim.* **28** 9013–28

Mao R, Gong D and Fang Q 2007 Influences of the East Asian jet stream on winter climate in China (in Chinese) *J. Appl. Meteorol. Sci.* **18** 137–46 (available at: http://qikan.camscma.cn/article/id/20070226)

Miao J, Wang T, Wang H, Zhu Y and Sun J 2018 Interdecadal weakening of the East Asian winter monsoon in the Mid-1980s: the roles of external forcings *J. Clim.* **31** 8985–9000

Monerie P-A, Wainwright C M, Sidibe M and Akinsanola A A 2020 Model uncertainties in climate change impacts on Sahel precipitation in ensembles of CMIP5 and CMIP6 simulations *Clim. Dyn.* **55** 1385–401

Nijsse F J M M, Cox P M and Williamson M S 2020 Emergent constraints on transient climate response (TCR) and equilibrium climate sensitivity (ECS) from historical warming in CMIP5 and CMIP6 models *Earth Syst. Dyn.* **11** 737–50

Peng Q, Xie S-P, Wang D, Huang R X, Chen G, Shu Y, Shi J-R and Liu W 2022 Surface warming–induced global acceleration of upper ocean currents *Sci. Adv.* **8** eabj8394

Rayner N A, Parker D E, Horton E B, Folland C K, Alexander L V, Rowell D P, Kent E C and Kaplan A 2003 Global analyses of sea surface temperature, sea ice, and night marine air temperature since the late nineteenth century *J. Geophys. Res. Atmos.* **108** 4407

Rose B E J, Armour K C, Battisti D S, Feldl N and Koll D D B 2014 The dependence of transient climate sensitivity and radiative feedbacks on the spatial pattern of ocean heat uptake *Geophys. Res. Lett.* **41** 1071–8

Rose B E J and Rayborn L 2016 The effects of ocean heat uptake on transient climate sensitivity *Curr. Clim. Change Rep.* **2** 190–201

Santer B D, Wigley T L, Schlesinger M E and Mitchell J F B 1990 *Developing Climate Scenarios from Equilibrium GCM Results* (available at: https://api.semanticscholar.org/CorpusID:127017512)

Schlund M, Lauer A, Gentine P, Sherwood S C and Eyring V 2020 Emergent constraints on equilibrium climate sensitivity in CMIP5: do they hold for CMIP6? *Earth Syst. Dyn.* **11** 1233–58

Shiogama H, Watanabe M, Kim H and Hirota N 2022 Emergent constraints on future precipitation changes *Nature* **602** 612–6

Shukla J and Mintz Y 1982 Influence of land-surface evapo-transpiration on the earths climate *Science* **215** 1498–501

Sun J, Wu S and Ao J 2016 Role of the North Pacific sea surface temperature in the East Asian winter monsoon decadal variability *Clim. Dyn.* **46** 3793–805

Tebaldi C and Arblaster J M 2014 Pattern scaling: its strengths and limitations, and an update on the latest model simulations *Clim. Change* **122** 459–71

Toda M and Watanabe M 2020 Mechanisms of enhanced ocean surface warming in the Kuroshio region for 1951–2010 *Clim. Dyn.* **54** 4129–45

Tokarska K B, Stolpe M B, Sippel S, Fischer E M, Smith C J, Lehner F and Knutti R 2020 Past warming trend constrains future warming in CMIP6 models *Sci. Adv.* **6** eaaz9549

Wang B, Wu Z, Chang C-P, Liu J, Li J and Zhou T 2010 Another look at interannual-to-interdecadal variations of the East Asian winter monsoon: the northern and southern temperature modes *J. Clim.* **23** 1495–512

Wang L and Chen W 2014 The East Asian winter monsoon: re-amplification in the mid-2000s *Chin. Sci. Bull.* **59** 430–6

Xu Y, Li J and Fu H 2022 The role of sea surface temperature variability in changes to global surface air temperature related to two periods of warming slowdown since 1940 *Clim. Dyn.* **59** 499–517

Xue D, Lu J, Leung L R, Teng H, Song F, Zhou T and Zhang Y 2023 Robust projection of East Asian summer monsoon rainfall based on dynamical modes of variability *Nat. Commun.* **14** 3856

Yang H, Lu J, Wang Q, Shi X and Lohmann G 2022 Decoding the dynamics of poleward shifting climate zones using aqua-planet model simulations *Clim. Dyn.* **58** 3513–26

Yao S-L, Luo J-J and Huang G 2016 Internal variability-generated uncertainty in East Asian climate projections estimated with 40 CCSM3 ensembles *PLoS One* **11** e0149968

Zhou S, Huang G and Huang P 2020 Inter-model spread of the changes in the East Asian summer monsoon system in CMIP5/6 models *J. Geophys. Res. Atmos.* **125** 2020JD033016

Zhou T and Yu R 2006 Twentieth-century surface air temperature over China and the globe simulated by coupled climate models *J. Clim.* **19** 5843–58